Systems/Circuits

Dendritic Organization of Olfactory Inputs to Medial Amygdala Neurons

Sepideh Keshavarzi, John M. Power, Eva H. H. Albers, Robert K. S. Sullivan, and Pankaj Sah
Queensland Brain Institute, The University of Queensland, St. Lucia, Queensland 4072, Australia

The medial amygdala (MeA) is a central hub in the olfactory neural network. It receives vomeronasal information directly from the accessory olfactory bulb (AOB) and main olfactory information largely via odor-processing regions such as the olfactory cortical amygdala (CoA). How these inputs are processed by MeA neurons is poorly understood. Using the GAD67-GFP mouse, we show that MeA principal neurons receive convergent AOB and CoA inputs. Somatically recorded AOB synaptic inputs had slower kinetics than CoA inputs, suggesting that they are electrotonically more distant. Field potential recording, pharmacological manipulation, and Ca^{2+} imaging revealed that AOB synapses are confined to distal dendrites and segregated from the proximally located CoA synapses. Moreover, unsynchronized AOB inputs had significantly broader temporal summation that was dependent on the activation of NMDA receptors. These findings show that MeA principal neurons process main and accessory olfactory inputs differentially in distinct dendritic compartments.

Key words: **dendrite; emotion; mating; olfaction; reproduction**

Significance Statement

In most vertebrates, olfactory cues are processed by two largely segregated neural pathways, the main and accessory olfactory systems, which are specialized to detect odors and nonvolatile chemosignals, respectively. Information from these two pathways ultimately converges at higher brain regions, one of the major hubs being the medial amygdala. Little is known about how olfactory inputs are processed by medial amygdala neurons. This study shows that individual principal neurons in this region receive input from both pathways and that these synapses are spatially segregated on their dendritic tree. We provide evidence suggesting that this dendritic segregation leads to distinct input integration and impact on neuronal output; hence, dendritic mechanisms control olfactory processing in the amygdala.

Introduction

Despite growing interest in understanding the mechanisms of emotional processing in the amygdala, our knowledge of this brain region is largely limited to those neural circuits that process multimodal sensory information and engage in acquired emotions, particularly conditioned fear (Phelps and LeDoux, 2005; Pare and Duvarci, 2012). However, a significant proportion of the amygdala, including the medial and the cortical nuclei, are dedicated to innate emotional processes, which, particularly in rodents, heavily depend on olfaction (Stowers et al., 2013).

Innate reproductive (e.g., mating and maternal) and defensive (e.g., predator avoidance or aggression) behaviors are central to survival, and the medial nucleus of the amygdala (MeA) is a key component of the neural circuits that drive these behaviors by relaying olfactory information to the behavior control column of the hypothalamus (Lehman et al., 1980; Fernandez-Fewell and Meredith, 1994; Canteras et al., 1995; Swanson, 2000; McGregor et al., 2004; Choi et al., 2005). The major input to the MeA is provided by the vomeronasal (or accessory olfactory) system via direct projections from mitral/tufted cells of the accessory olfactory bulb (AOB; Scalia and Winans, 1975; von Campenhausen and Mori, 2000; Mohedano-Moriano et al., 2007). This input conveys information about chemosignals that trigger innate reactions, namely, pheromones and kairomones (Ben-Shaul et al., 2010; Papes et al., 2010). Odor information, on the other hand, reaches the MeA mainly via higher-order projections from the

Received Feb. 15, 2015; revised July 21, 2015; accepted Aug. 12, 2015.

Author contributions: S.K. and P.S. designed research; S.K., J.M.P., E.H.H.A., and R.K.S.S. performed research; S.K. analyzed data; S.K. and P.S. wrote the paper.

This work was supported by grants from the National Health and Medical Research Council of Australia and the Australian Research Council (P.S.) and scholarship from the University of Queensland (S.K.). We thank Alan Woodruff for comments on this manuscript.

The authors declare no competing financial interests.

Correspondence should be addressed to Pankaj Sah, Queensland Brain Institute, Building 79, The University of Queensland, St. Lucia, QLD 4072, Australia. E-mail: pankaj.sah@uq.edu.au.

S. Keshavarzi's present address: Division of Neurophysiology, MRC National Institute for Medical Research, The Ridgeway, Mill Hill, London NW7 1AA, United Kingdom.

DOI:10.1523/JNEUROSCI.0627-15.2015

 0270-6474/15/3513020-09$15.00/0

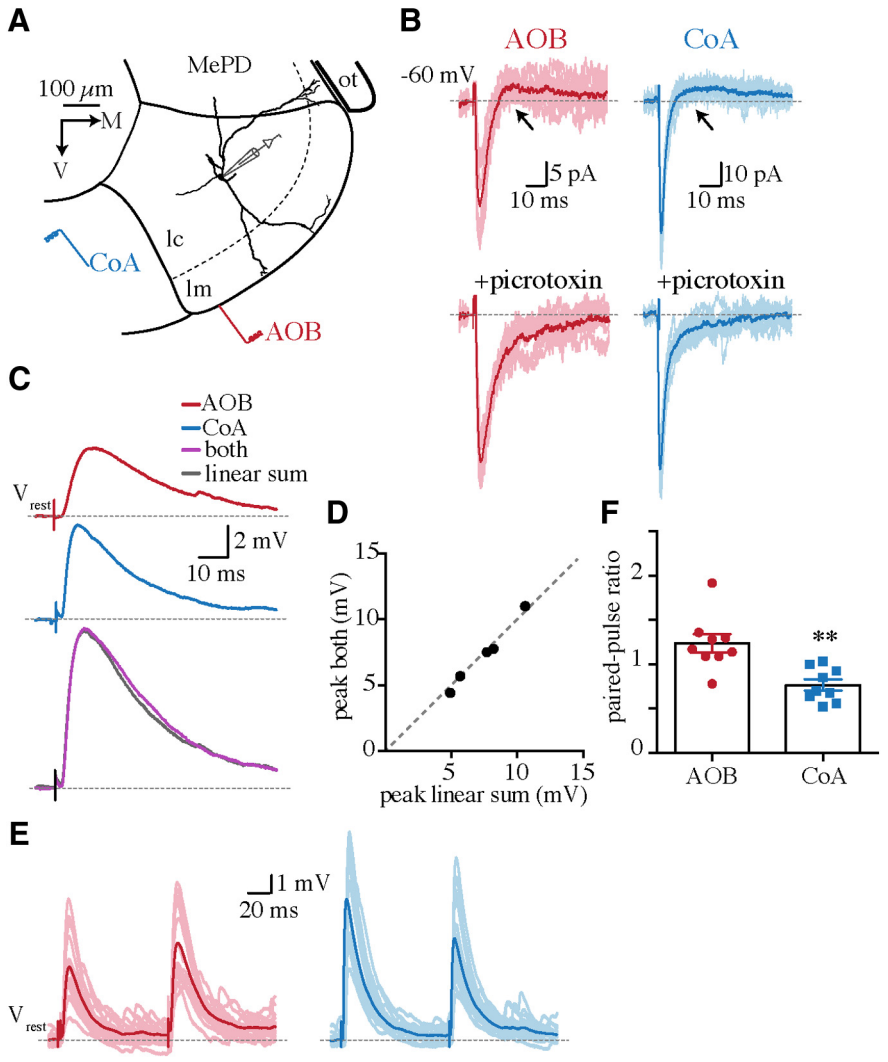

Figure 1. MePV neurons receive convergent AOB and CoA synaptic inputs. ***A***, Schematic of MePV boundaries with a superimposed reconstructed GFP-negative neuron in the cellular layer (lc). AOB and CoA synaptic inputs were evoked by electrical stimulation of the ventral surface of the molecular layer (lm) and the olfactory CoA, respectively. MePD, Posterodorsal medial amygdala; ot, optic tract. ***B***, AOB (red) and CoA (blue) evoked postsynaptic currents ($V_{hold} = -60$ mV) before (top) and after (bottom) applying the $GABA_A$-receptor antagonist picrotoxin (100 μM). Arrows indicate delayed IPSCs. ***C***, Averaged AOB (red) and CoA (blue) EPSPs and the response to simultaneous stimulation of both inputs (purple) in a representative cell. The gray trace is the algebraic sum of the two individual traces (red plus blue). ***D***, The peak amplitude of the algebraic sum plotted against that of simultaneously evoked responses. Each dot represents ensemble-averaged EPSPs in one cell. Note that data points are close to unity (dashed line). ***E***, ***F***, AOB (red) and CoA (blue) EPSPs evoked by two successive electrical stimuli in a representative cell (***E***) and mean ± SEM paired-pulse ratio for the two inputs (***F***; $n = 9$ neurons). $^{**}p < 0.01$ (unpaired Student's *t* test).

olfactory cortices such as the piriform cortex and the olfactory cortical amygdala (CoA; anterior and posterolateral divisions), although minor direct projections from the main olfactory bulb (MOB) to the rostral divisions of the MeA have also been described (Kevetter and Winans, 1981; McDonald, 1998; Pro-Sistiaga et al., 2007; Kang et al., 2009; Martinez-Marcos, 2009; Miyamichi et al., 2011; Sosulski et al., 2011; Bergan et al., 2014; Cádiz-Moretti et al., 2014).

As a major site of convergence of the largely nonoverlapping main and accessory olfactory pathways, the MeA is well positioned to integrate chemosensory information detected by different olfactory systems (Brennan and Zufall, 2006; Martinez-Marcos, 2009). However, little is known about the neural basis of olfactory processing in this region. Data from *in vivo* single unit recordings (Bergan et al., 2014) and immediate early gene expressions (Samuelsen and Meredith, 2009) suggest that MeA neurons can be driven by vomeronasal but not main olfactory input. In contrast, a previous study (Licht and Meredith, 1987) showed that stimulation of either the MOB or the vomeronasal organ can drive the same neurons in the posteromedial cortical amygdala, another vomeronasal processing region adjacent to the MeA. Thus, whether individual MeA neurons receive convergent inputs from the two olfactory pathways remains unclear, particularly considering that extracellular unit activity (Licht and Meredith, 1987; Binns and Brennan, 2005; Bergan et al., 2014; Govic and Paolini, 2015) reports neuronal output without providing any information about subthreshold synaptic inputs to individual neurons. Furthermore, the physiological properties of these inputs and their synaptic organization in the MeA are little understood (Bian et al., 2008; Keshavarzi et al., 2014). Here, we studied the responses of principal neurons in the posteroventral division of the MeA (MePV) to stimulation of olfactory CoA and AOB afferents, representing the main and accessory olfactory pathways, respectively. The MePV was chosen because of its anatomical proximity to both AOB afferents and the olfactory CoA as well as the clear segregation of main and accessory olfactory bulb projections at posterior regions (Martinez-Marcos, 2009), which facilitates independent stimulation of the two inputs in slice preparations. MePV principal neurons were found to receive convergent AOB and CoA inputs that are differentially segregated on their dendritic tree. We find that, compared to CoA inputs, AOB inputs are located on the distal dendritic arbor and show a broader summation and higher output gain. These findings suggest distinct processing of main and accessory olfactory information by MeA neurons.

Materials and Methods

Slice preparation and electrophysiology. Acute brain slices were prepared from 35- to 50-d-old male heterozygous *GAD67-EGFP* (Δneo) mice (referred to as *GAD67-GFP* mice), in which enhanced green fluorescent protein is expressed under the control of the promoter for the GABA synthesizing enzyme, GAD67 (Tamamaki et al., 2003). The exclusive use of males was designed to minimize the effect of sex and hormonal variations in the sexually dimorphic MeA (Rasia-Filho et al., 2004; Cooke and Woolley, 2005; Cooke et al., 2007). Following deep isoflurane anesthesia, mice were decapitated in accordance with the guidelines of the University of Queensland Animal Ethics Committee. Brains were rapidly removed and placed into ice-cold, oxygenated (bubbled with 95% O_2/5% CO_2) cutting solution containing the following (in mM): 87 NaCl, 50 sucrose,

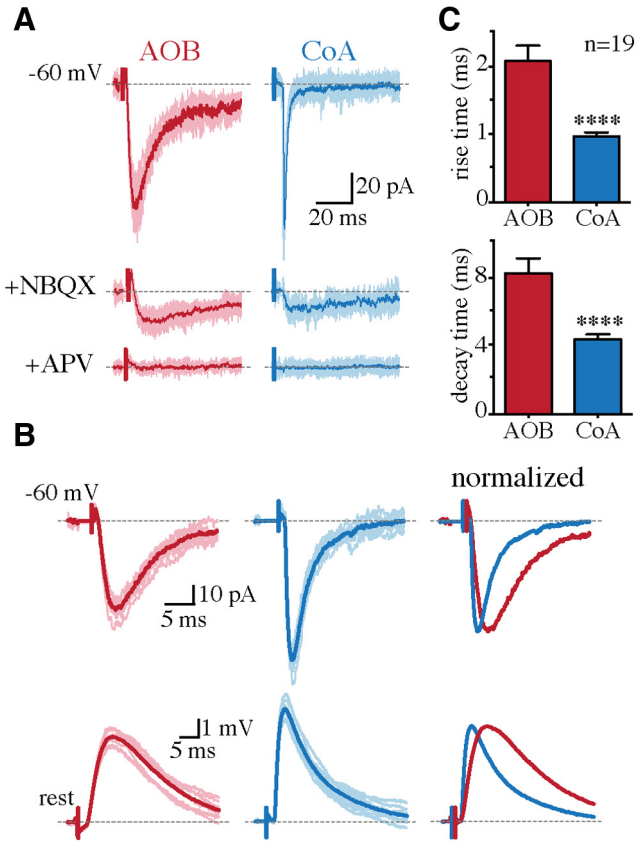

Figure 2. AOB inputs have slower rise and decay kinetics than CoA inputs. ***A***, AOB and CoA EPSCs ($V_{hold} = -60$ mV) in a representative MePV cell in the presence of picrotoxin (top) and after serial NBQX (10 μM; middle) and D-APV (30 μM; bottom) application. Traces in lighter shades are individual responses, with the averaged responses superimposed in dark red (AOB) and blue (CoA). ***B***, EPSCs (top) and potentials (bottom) in a representative cell evoked by AOB (red) and CoA (blue) stimulation, and the overlaid averaged responses (right) normalized to the response peak. ***C***, Rise time (top) and decay time constant (bottom) of evoked EPSCs (mean ± SEM; $V_{hold} = -60$ mV; $n = 19$ cells). ****$p < 0.0001$ (unpaired Student's t test).

25 glucose, 25 $NaHCO_3$, 2.5 KCl, 4 $MgCl_2$, 0.5 $CaCl_2$, and 1.2 NaH_2PO_4. Coronal slices (300 μm thick) were prepared using a vibrating microslicer (Leica) and incubated at 35°C for 30 min in oxygenated artificial CSF (ACSF) containing the following (in mM): 118 NaCl, 10 glucose, 25 $NaHCO_3$, 2.5 KCl, 1.3 $MgCl_2$, 2.5 $CaCl_2$, and 1.2 NaH_2PO_4. Slices were then allowed to equilibrate at room temperature for at least 30 min before being transferred to the recording chamber.

During recordings, slices were superfused with oxygenated ACSF maintained at 32–34°C. Recording electrodes (3–5 MΩ) were prepared from borosilicate glass and filled with internal solution containing the following (in mM): 135 $KMeSO_4$, 8 NaCl, 10 HEPES, 2 Mg_2-ATP, 0.3 Na_3-GTP, and 0.3 EGTA (pH 7.3 with KOH; osmolarity, ~290 mOsm). Biocytin (0.3%) was added to the internal solution in some recordings. Whole-cell patch-clamp recordings were made from the soma of GFP-negative neurons in the MePV (Bregma, −1.34 to −1.82 mm; Paxinos and Franklin, 2001) using infrared differential interference contrast video microscopy (Stuart et al., 1993) with an upright microscope (BX50WI, Olympus) equipped with fluorescence attachments. Cells with a resting membrane potential more positive than −55 mV and an access resistance >20 MΩ were discarded. Current- or voltage-clamp recordings were made using a patch-clamp amplifier (MultiClamp 700B, Molecular Devices), low-pass filtered at 6 kHz, and digitized at 20 kHz using an ITC-16 interface board (Instrutech) under the control of Axograph X (version 1.4.4, Axograph Scientific). For extracellular recordings, borosilicate glass micropipettes with a smaller tip size (5–7 MΩ), which were filled with a sodium chloride solution (3M), were used. Extracellular signals were low-pass filtered at 1–2 kHz and sampled at 10 kHz.

A theta glass or a custom-built silver-coated bipolar stimulating electrode (~2–5 μm tip diameter, filled with ACSF) was used for electrical stimulations. AOB afferents and the olfactory CoA were alternately stimulated (interval, 1 s; pulse duration, 100–300 μs; frequency, 0.1–0.2 Hz) by two stimulating electrodes, placed in the ventral surface of the MeA molecular layer (Bian et al., 2008; Keshavarzi et al., 2014) and in the posterolateral or anterior CoA (Bregma, −1.34 to −1.82 mm; Paxinos and Franklin, 2001), respectively (Fig. 1*A*). The molecular layer of the MeA is a well-defined cell-sparse region located at its external ventromedial borders (Keshavarzi et al., 2014, their Fig. S1*A*) and contains dense axonal projections from mitral/tufted cells of the AOB (von Campenhausen and Mori, 2000; Mohedano-Moriano et al., 2007). Stimulation intensities (10–40 V) were adjusted to evoke EPSPs of either minimal or ~20–50% maximal amplitude. To measure the paired-pulse ratio (PPR), two successive stimuli were delivered at a 100 ms interval. To evoke a train of EPSPs, short trains of stimuli (5–10 stimuli at 50 Hz) were delivered at 0.1–0.2 Hz.

Pharmacology. Tetrodotoxin (TTX; 1 μM) was pressure applied focally (500 kPa; 300 ms) with a glass electrode (5–6 MΩ) attached to a Picospritzer II (General Valve). The electrode was placed close to the distal dendritic branches in the molecular layer, which were visualized by addition of the fluorescent dye Alexa Fluor 568 (Invitrogen; 10 μM) to the internal solution. To monitor the flow of TTX in the slice, Alexa Fluor 568 was also included in the puffing electrode together with TTX. The position of the puffing electrode and the bath circulation were adjusted to allow the flow of TTX toward the suction and away from the tissue and stimulation sites. All other drugs were bath applied at the following concentrations (in μM): 50 baclofen (Sigma), 30 D-APV (Sigma), 10 NBQX (Tocris), and 100 picrotoxin (Sigma).

Morphology reconstruction. Morphology of some recorded neurons ($n = 10$) was visualized using streptavidin-conjugated fluorescent dyes as described previously (Keshavarzi et al., 2014). Briefly, slices containing biocytin-filled cells were fixed in 4% paraformaldehyde in 0.1 M phosphate buffer (PB), pH 7.4, for 1 h. Following washes in 0.1 M PBS containing 0.3% Triton X-100 (three times, 10 min each), slices were incubated in streptavidin-conjugated Alexa Fluor 568 or 647 (1:1000; Invitrogen) for 5 h. They were then washed with PBS and mounted with 50% glycerol in PBS. Fluorescent images were acquired using a confocal microscope, and morphology reconstructions were made with Neurolucida (MBF Bioscience).

Two-photon calcium imaging. The green fluorescent calcium indicator Oregon Green BAPTA-1 (OGB-1; 100 μM; Invitrogen) and the red fluorescent calcium-insensitive Alexa Fluor 594 (30 μM; Invitrogen) were added to the internal solution (made without EGTA). After establishing whole-cell configuration, dyes were allowed to diffuse into the dendrites for at least 10 min before starting calcium imaging. Subthreshold AOB or CoA EPSPs were evoked by 50 Hz trains of electrical stimulation, and data were excluded if synaptically driven spikes were observed. Two-photon images of OGB-1 and Alexa Fluor 594 were acquired using a Zeiss LSM 710 equipped with a Chameleon multiphoton imaging laser (Coherent) at an excitation wavelength of 810 nm. The emitted light was split with a dichroic filter, bandpass filtered (green channel, 500–550 nm; red channel, 565–610 nm), and detected with separate nondescanned detectors. Fluorescence images were obtained in line-scan mode (200–300 Hz) at a resolution of 10–20 pixels/μm. Line scans were performed orthogonal to the dendritic shaft and, in some cases, included the attached spines. Calcium signals in spines and the parent dendritic shafts were pooled. Image analysis was performed off-line using custom-written procedures in Fiji (Schindelin et al., 2012). The z-stack images were taken at the conclusion of the experiments and used to measure the distance of scanned sites from the soma. Calcium signals were quantified as the change in the green fluorescence (ΔG) divided by the red fluorescence (R). Only $\Delta G/R$ changes larger than three times the standard deviation of the baseline noise were considered as calcium transient. $\Delta G/R$ traces were plotted in Axograph, averaged (three to five traces), and postfiltered at 10–20 Hz to improve visibility.

Electrophysiological analysis. Electrophysiological analysis was performed using Axograph X. For measurements of synaptic events, ensemble-averaged responses from a minimum of five sweeps were used.

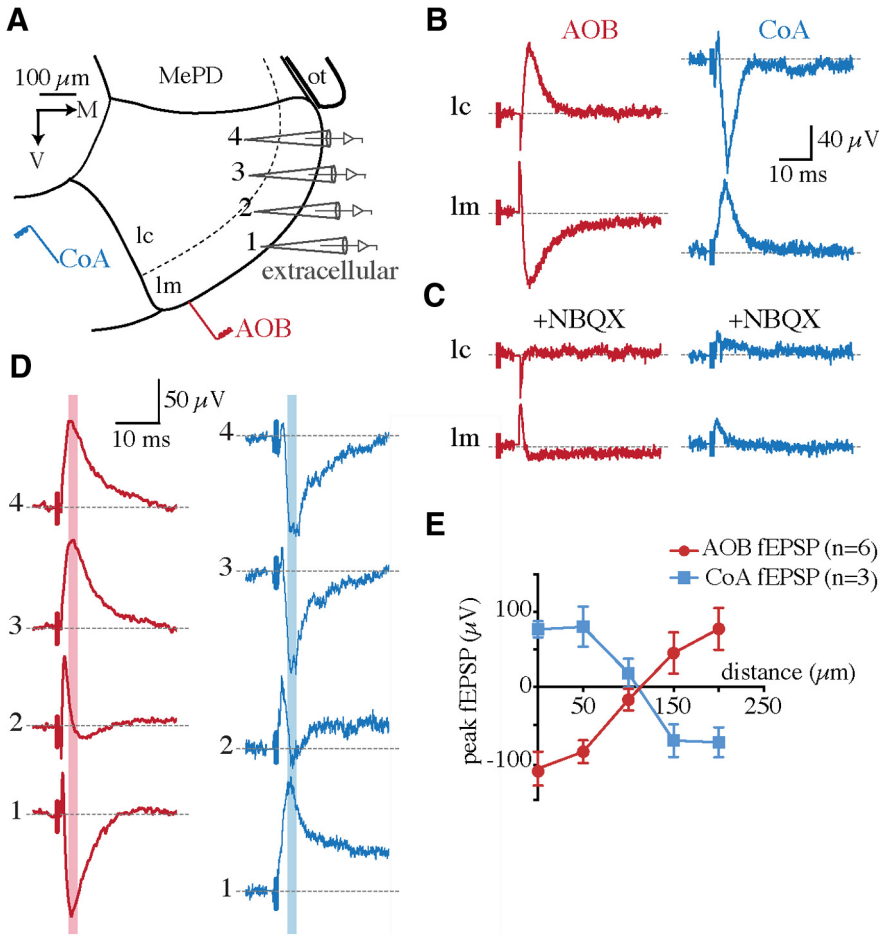

Figure 3. AOB and CoA field potentials have different spatial profiles in the MePV. ***A***, Schematic of field recordings. The extracellular electrode was moved from ventral [1 in the molecular layer (lm)] to dorsal [4 in the cellular layer (lc)] locations while AOB and/or CoA afferents were stimulated. MePD, Posterodorsal medial amygdala; ot, optic tract. ***B***, Field potentials evoked by electrical stimulation of AOB (red) and CoA (blue) afferents in the presence of picrotoxin (100 μM). Traces are averaged responses recorded extracellularly in the cellular and molecular layers. Both recordings were made in the same slice. ***C***, The same recordings as in ***B***, after bath application of NBQX (10 μM). ***D***, Representative averaged AOB and CoA fEPSPs recorded at locations shown in ***A***. ***E***, The peak amplitude of fEPSPs (mean ± SEM) at each location, marked with pink and blue lines in ***D***, was plotted against the distance of the recording electrode from the ventral surface of the MeA. *n* is the number of recordings (one slice was recorded in each mouse, with a total of 6 slices). In three slices, only AOB fEPSPs were recorded. In all other slices with CoA field recordings, AOB fEPSPs were also evoked with a second stimulating electrode.

The onset of evoked EPSCs was measured as the delay between the stimulus artifact and the foot of the EPSC. The EPSC decay time constant was measured by a single exponential fit to the current decay at −60 mV holding potential. The EPSC rise time was measured from 10 to 90% of the EPSC peak amplitude. The PPR was calculated by dividing the peak amplitude of the second EPSP to that of the first. EPSP summation was measured as the area under the EPSP train waveform (integral of EPSP trains) normalized to that of a single EPSP.

Statistical analysis. Statistical comparisons and graphs were made using Prism 6 (GraphPad). Data are presented as means ± SEM. Unless stated otherwise, a Student's two-tailed *t* test (paired or unpaired) or a two-way ANOVA with a Bonferroni correction was used for comparisons between groups. Differences were considered statistically significant at $p < 0.05$.

Results

Whole-cell recordings were obtained from principal neurons in acute brain slices prepared from *GAD67-GFP* mice (Keshavarzi et al., 2014). The majority of MePV principal neurons are glutamatergic (Choi et al., 2005; Bian et al., 2008) and were distinguished from GABAergic neurons by the absence of GFP fluorescence (Bian et al., 2008; Keshavarzi et al., 2014). We first tested whether MePV neurons receive convergent inputs from the AOB and the olfactory CoA. Stimulation of either CoA or AOB afferents (Fig. 1*A*; see Materials and Methods) reliably evoked monosynaptic EPSCs in every cell (mean EPSC amplitude, AOB, 55 ± 10 pA; CoA, 54 ± 5 pA; V_{hold}, −60 mV; $n = 27$; Fig. 1*B*), showing that these two inputs converge onto individual neurons. Evoked synaptic currents were generally followed by a disynaptic inhibitory component (Fig. 1B; 76% of AOB and 78% of CoA inputs), which is likely mediated by local circuit GABAergic interneurons (Bian et al., 2008; Keshavarzi et al., 2014). Monosynaptic AOB and CoA inputs were therefore isolated using picrotoxin to block inhibition (Fig. 1*B*). In current clamp, stimulation of AOB or CoA afferents evoked subthreshold EPSPs, and the algebraic sum of the peak amplitudes of the two evoked inputs was equal to that of the simultaneously evoked EPSP, consistent with the absence of shared fibers between the two inputs (Fig. 1*C*,*D*). Linear summation was observed over a broad range of stimulation intensities (10–40 V), which evoked EPSPs of varying sizes (peak amplitude, AOB, 1.8 to 4 mV; CoA, 3.1 to 6.8 mV). Moreover, whereas AOB EPSPs mostly showed paired-pulse facilitation (paired-pulse ratio, AOB, 1.2 ± 0.1), CoA inputs displayed paired-pulse depression (paired-pulse ratio, 0.8 ± 0.06; $n = 9$; $p < 0.01$; Fig. 1*E*,*F*), confirming the independence of these inputs.

For both inputs, application of the selective AMPA/kainate receptor antagonist NBQX (10 μM; $n = 5$) blocked the fast component of the EPSC, and the remaining slower component was blocked by the NMDA receptor (NMDAR) antagonist D-APV (30 μM; $n = 5$; Fig. 2*A*). Thus, both AOB and CoA inputs make dual component glutamatergic synapses on MeA principal neurons. However, the kinetics of AOB-evoked AMPA-receptor-mediated EPSCs were significantly different from those evoked by CoA input, with both the rising phase (EPSC 10–90% rise time, AOB, 2 ± 0.2 ms; CoA, 1 ± 0.06 ms; $n = 19$; $p < 0.0001$) and deactivation kinetics (EPSCs decay time constant, AOB, 8 ± 0.8 ms; CoA, 4 ± 0.3 ms; V_{hold}, −60 mV; $n = 19$; $p < 0.0001$) being significantly slower for AOB inputs (Fig. 2*B*,*C*). What accounts for this difference in EPSC kinetics? One possible explanation could be that the two inputs are located at distinct dendritic locations, with electrotonic filtering accounting for the difference in their kinetics (Rall, 1967; Magee and Cook, 2000; Williams and Stuart, 2002). Morphological reconstruction of biocytin-filled neurons ($n = 10$) showed that in all cells, at least one primary dendrite extends to the molecular layer, where it forms distal branches (Fig. 1*A*; Keshavarzi et al., 2014). Considering the dense AOB projections to the molecular layer

(von Campenhausen and Mori, 2000; Mohedano-Moriano et al., 2007), it is likely that AOB synapses are formed at these distal branches and are hence more electrotonically remote from the soma than the putatively proximal CoA synapses.

We first tested this hypothesis using extracellular field recordings. If AOB synapses were distal and CoA synapses proximal, the evoked field potentials would have a laminar profile, with the current sink of the AOB input in the molecular layer and that of the CoA input in the cellular layer (Colbert and Levy, 1992). Extracellular field recordings were made at different depths of the MePV by moving the recording electrode from the molecular to the cellular layer while AOB or CoA afferents were electrically stimulated (Fig. 3*A*). Field EPSPs (fEPSPs) could be evoked by both AOB and CoA stimulation and were fully blocked by NBQX (10 μM; $n = 4$; Fig. 3*B*,*C*), confirming their synaptic origin. In agreement with a differential anatomical location of these inputs, fEPSPs evoked by AOB and CoA stimulation had opposite polarities (Fig. 3*B*,*D*); the sink (negativity) of AOB fEPSPs (peak, -117 ± 16 μV; $n = 14$) was in the molecular layer, whereas that of the CoA input (peak, -79 ± 14 μV; $n = 10$) was in the cellular layer (Fig. 3). Interestingly, the polarity of both fEPSPs reversed at ~100–150 μm from the ventral surface of the MeA (Fig. 3*D*,*E*), corresponding to the depth of the molecular layer (Fig. 3*A*; Keshavarzi et al., 2014). These data suggested that AOB and CoA synapses have distinct spatial distributions in MeA principal neurons. To directly confirm this prediction, we used focal pharmacology on individual neurons to test whether disruption of synaptic transmission at distal dendrites could block the AOB but not the CoA synaptic inputs. Whole-cell recordings were made from MePV principal neurons and their dendrites visualized by addition of Alexa Fluor 568 in the internal solution. Focal pressure ejection of TTX (1 μM) onto distal dendritic branches in the molecular layer (Fig. 4*A*) substantially blocked AOB EPSCs (81 ± 0.6% block), with minimal effect on the CoA input (8 ± 0.5% block; $n = 8$; AOB vs CoA, $p < 0.0001$; Fig. 4*B*,*C*), showing that these two inputs are differentially segregated on individual neurons.

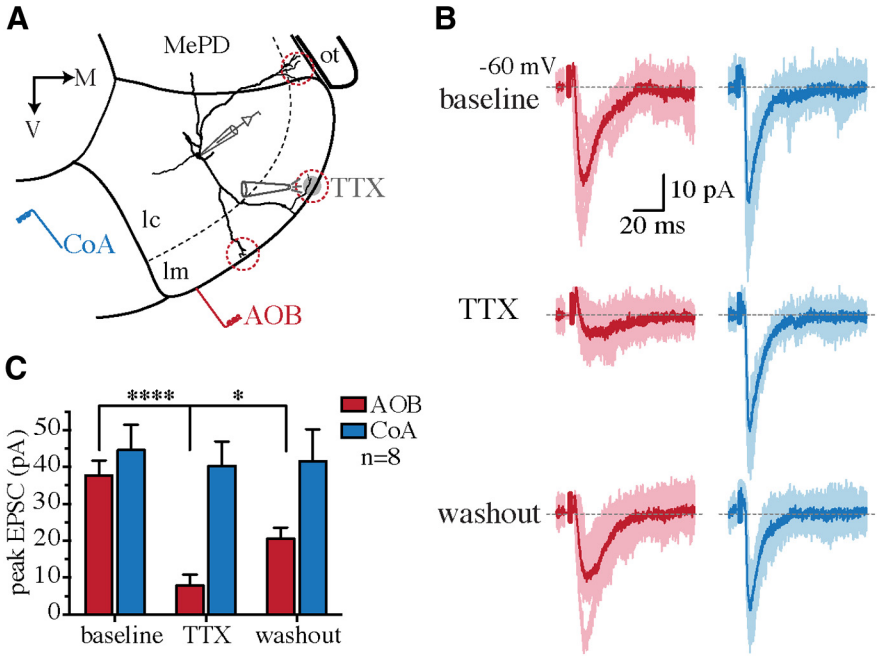

Figure 4. Focal blockade of synaptic transmission at distal dendrites disrupts AOB but not CoA inputs. ***A***, Schematic of focal pressure application of TTX at distal dendritic branches (red circles) of MePV principal neurons. MePD, Posterodorsal medial amygdala; ot, optic tract; lm, molecular layer; lc, cellular layer. ***B***, AOB (red) and CoA (blue) EPSCs ($V_{hold} = -60$ mV) recorded before (top) and after (middle) puffing 1 μM TTX at distal dendrites and following washout (bottom). Whereas AOB EPSCs were blocked by TTX (left), CoA input remained intact (right). ***C***, Summary data showing the effect of focal TTX application on the peak amplitude of evoked EPSCs (mean ± SEM; $n = 8$ cells). *$p < 0.05$; ****$p < 0.0001$ (two-way ANOVA with Bonferroni's test).

To elucidate the subcellular distribution of AOB and CoA synapses, we next performed two-photon Ca^{2+} imaging and mapped these inputs on dendrites of MePV principal neurons. Whole-cell recordings were made with the red fluorescent Alexa Fluor 594 and the green fluorescent Ca^{2+} indicator OGB-1 (100 μM) in the internal solution. A train of AOB or CoA EPSPs (50 Hz; 5–10 stimuli) was evoked, and dendrites extending toward the molecular layer were scanned at different distances from the soma (Fig. 5*A*,*D*). Dendritic Ca^{2+} transients were reliably evoked by subthreshold AOB EPSPs (10 of 12 neurons), with the largest rise at the most distal locations (somatic distance, 183 ± 16 μm; $\Delta G/R = 8 \pm 1$%; $n = 10$). These transients sharply attenuated at more proximal sites (129 ± 15 μm; $\Delta G/R = 2 \pm 0.9$%; $n = 10$) and were absent close to the soma (Fig. 5*A*,*B*,*F*,*I*). Conversely, when high-frequency (100 Hz) bursts of action potentials (APs) were evoked by somatic current injection, Ca^{2+} signals were readily observed in proximal dendrites (38 ± 5 μm; $\Delta G/R = 29 \pm 4$%; $n = 8$; Fig. 5*C*), showing that the absence of AOB-evoked transients at these sites was not due to a phototoxic damage or loss of their physiological function. Moreover, similar to hippocampal CA1 and cortical pyramidal neurons (Spruston et al., 1995; Helmchen et al., 1999; Bathellier et al., 2009), Ca^{2+} transients evoked by these high-frequency APs substantially declined at distal dendrites (183 ± 23 μm; $\Delta G/R = 9 \pm 3$%; $n = 8$; Fig. 5*C*,*H*), suggesting attenuation of backpropagating APs. In four cells, dendrites that extended in the lateral/dorsolateral direction were also tested, but no AOB-evoked Ca^{2+} signal was detected in these branches; thus, AOB synapses appear to be confined to the distal dendrites located in the molecular layer. In contrast, CoA EPSPs generated Ca^{2+} transients in proximal dendritic domains (somatic distance, 34 ± 9 μm; $\Delta G/R = 5 \pm 2$%; $n = 5$; Fig. 5*D*,*E*,*G*,*I*) of either the ventral/ventromedial ($n = 2$) or the lateral/dorsolateral ($n = 3$) dendrites.

The location of synapses on the dendritic arbor is known to shape the integration of synaptic inputs, their impact on neuronal output, and their plasticity (Magee, 2000; Williams and Stuart, 2003; London and Häusser, 2005; Kampa et al., 2007). To test whether the segregated AOB and CoA synaptic inputs integrate differently at the soma, we compared the temporal summation of asynchronous EPSPs at these two synapses. Trains of AOB and CoA EPSPs (50 Hz) were alternatively evoked at rest (-69 ± 2 mV) and summation calculated as the integral of waveform of the EPSPs normalized to that of a single EPSP. Stimulation intensities were adjusted to evoke individual EPSPs of either minimal (peak EPSP, AOB, 2 ± 0.2 mV; CoA, 3 ± 0.5 mV; $n = 8$) or ~50% maximal amplitude (peak EPSP, AOB, 6 ± 0.6 mV; CoA, 6 ± 0.2 mV; $n = 8$); however, because summation was similar at both intensities, data were pooled. Temporal summation of AOB

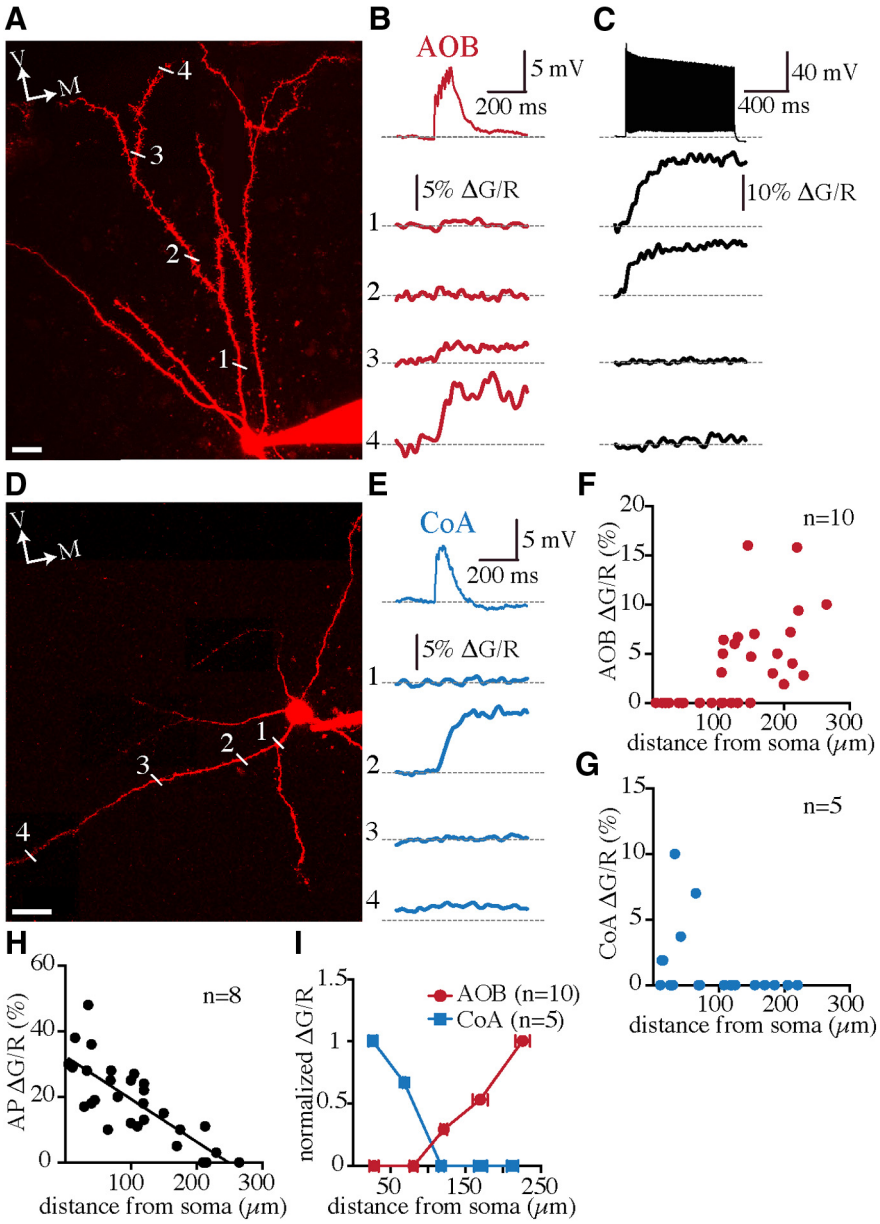

Figure 5. Ca^{2+} transients evoked by AOB and CoA inputs are confined to segregated dendritic locations. ***A***, Compressed *z*-stack two-photon image of an Alexa Fluor 594–filled GFP-negative MePV neuron scanned for AOB-evoked Ca^{2+} transients. The sites of line scan on a ventrally extending dendrite are labelled (1–4). ***B***, A 50 Hz train of EPSPs evoked by electrical stimulation of AOB afferents (top) and simultaneous recordings of Ca^{2+} transients (1–4; plotted as $\Delta G/R$) at dendritic locations shown in ***A***. ***C***, A 100 Hz train of APs (top) evoked by somatic current injection and simultaneous Ca^{2+} signals (1–4) recorded at the same dendritic sites shown in ***A***. ***D***, Compressed *z*-stack two-photon image of a GFP-negative MePV neuron scanned for CoA-evoked Ca^{2+} transients. The sites of line scan on a laterally extending dendrite are labelled (1–4). ***E***, A 50 Hz train of EPSPs evoked by electrical stimulation of the posterolateral CoA (top) and Ca^{2+} transients (1–4) recorded at dendritic locations shown in ***D***. ***F–H***, Population data of calcium transients evoked by 50 Hz trains of AOB (***F***) and CoA (***G***) EPSPs and a 100 Hz train of backpropagating action potentials (***H***) plotted against the distance from the soma. ***I***, $\Delta G/R$ values were binned at 50 μm distances from the soma, and the averaged $\Delta G/R$ values, calculated at each bin and normalized to the largest value, were plotted against the distance from the soma (mean ± SEM). V, Ventral; M, medial. *n*, Number of cells. Scale bars: 20 μm.

EPSPs was significantly greater than that of CoA EPSPs (20 ± 3 vs 7 ± 1; $n = 16$; $p < 0.01$; Fig. 6), which either failed to summate or showed little summation (Fig. 6*A*,*B*). Consequently, AOB EPSPs depolarized the soma closer to the AP threshold than did the CoA EPSPs (peak EPSP train-amplitude first EPSP, AOB, 6 ± 1 mV; CoA, 1 ± 0.6 mV; $n = 16$; $p < 0.001$) and were more likely to discharge the cell (spikes/EPSP train, 1 ± 0.3 vs 0; $n = 16$; $p < 0.05$; Fig. 6*A*). The larger temporal summation of AOB EPSPs can be partly explained by the slow decay of distal inputs as a result of passive dendritic filtering (Rall, 1964, 1967). Active dendritic conductances, such as voltage-gated Na^+ and Ca^{2+} channels and NMDAR, may also amplify the integration and gain of distal inputs (Schiller et al., 1997; Golding and Spruston, 1998; Larkum et al., 2009; Branco and Häusser, 2011). To test the contribution of NMDARs to temporal integration of AOB and CoA inputs, NMDARs were blocked using D-APV (30 μM; $n = 5$). Application of D-APV substantially suppressed the summation of AOB EPSPs and reduced the magnitude of somatic depolarization (Fig. 6*B–D*), but had little effect on CoA input summation, suggesting that NMDARs substantially enhance the integration and gain of AOB inputs.

Discussion

The medial nucleus of the amygdala plays a central role in generating innate behavioral responses to biologically relevant chemosignals (Lehman et al., 1980; Fernandez-Fewell and Meredith, 1994; Li et al., 2004; McGregor et al., 2004; Binns and Brennan, 2005; Brennan and Zufall, 2006; Samuelsen and Meredith, 2011; Bergan et al., 2014; Govic and Paolini, 2015). Olfactory information from the main and accessory olfactory pathways reach the MeA, where it is further processed and relayed to hypothalamic regions that control defensive and reproductive behaviors (Scalia and Winans, 1975; Canteras et al., 1995; Choi et al., 2005). Here we describe the processing of two distinct inputs conveying putative vomeronasal (AOB) and main olfactory information (olfactory CoA) to neurons in the posteroventral division of the MeA. We showed that inputs from these two olfactory pathways converge onto MeA principal neurons at different dendritic domains and display distinct temporal integration, with larger summation and higher output gain for AOB synapses. The GAD67-GFP mouse was used to facilitate the identification of principal (projection) neurons. We showed previously that all GFP− and most GFP+ neurons in the MePV of this mouse are projection cells (Keshavarzi et al., 2014). Moreover, previous data have confirmed that the majority of MePV projection neurons express VGlut2, and are thus glutamatergic (Choi et al., 2005; Bian et al., 2008). Hence, even if some GFP− cells in the present study are actively GABAergic, but lack a detectable level of GFP expression due to inactivity (Lau and Murthy, 2012), they are still most likely principal neurons.

It should be noted that the electrical stimulation in the molecular layer used in this study might have inadvertently recruited other fibers and contaminated these inputs. This

could have particularly affected the AOB input, which was evoked by stimulating the afferent fibers in the molecular layer of the MeA, rather than by direct stimulation of the AOB. However, previous anatomical data from comprehensive neural tracing experiments in the mouse brain show that afferents in the molecular layer are dominated by those arising in the AOB, and the majority of other afferents to the MeA do not contact the superficial molecular layer (Oh et al., 2014; Allen Mouse Brain Connectivity Atlas, http://connectivity.brain-map.org). Moreover, the small MOB projections that are present in the molecular layer mostly terminate in the rostral MeA and are negligible in slices containing the MePV (von Campenhausen and Mori, 2000; Pro-Sistiaga et al., 2007; Kang et al., 2009; Cádiz-Moretti et al., 2014; see also experiments 120812686 and 146921849 in the Allen Mouse Brain Connectivity Atlas, http://connectivity.brain-map.org). Hence, for the MePV, the contribution of non-AOB inputs when stimulating in the molecular layer would be minimal.

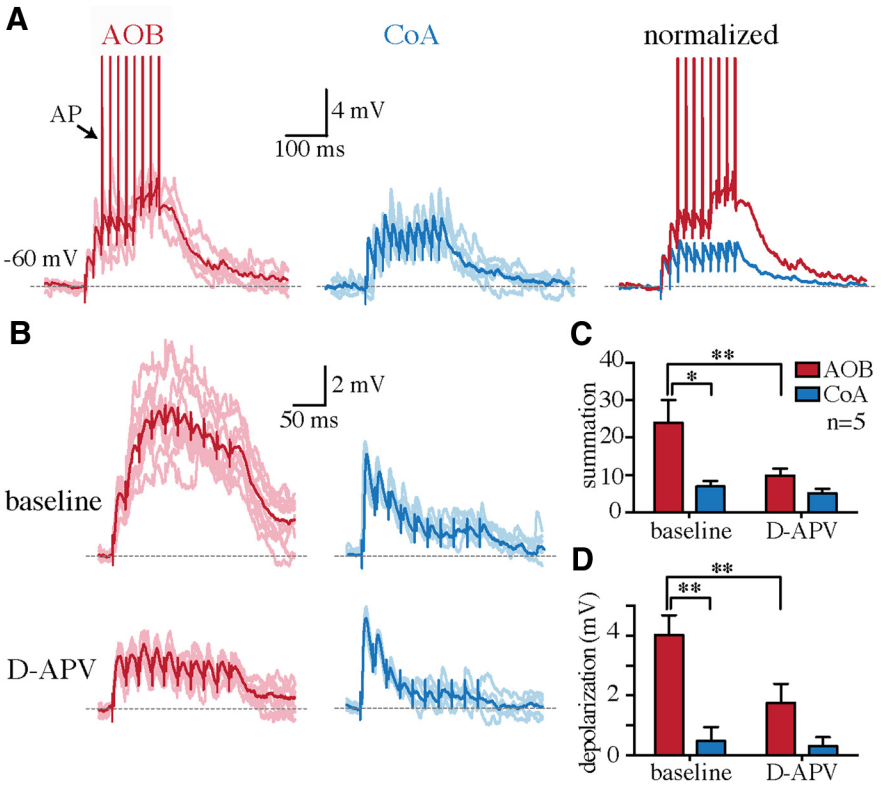

Figure 6. AOB synaptic inputs show a larger temporal summation than the CoA inputs. ***A***, Fifty hertz trains of AOB (red, left) and CoA (blue, middle) EPSPs evoked in a representative MePV principal neuron at resting membrane potential ($V_{rest} = -60$ mV). Overlaid traces (right) are normalized to the peak of the first EPSP. Summation of AOB EPSPs provided sufficient depolarization to generate action potentials (arrow, truncated APs). ***B***, Fifty hertz trains of AOB (red) and CoA (blue) EPSPs in a representative cell recorded before (top) and after application of 30 μM D-APV (bottom). ***C***, ***D***, AOB EPSPs showed a larger temporal summation (measured as the integral of the EPSP train divided by that of a single EPSP) than the CoA EPSPs (***C***), and thus depolarized the membrane potential (measured by subtracting the peak amplitude of the first EPSP from the peak of EPSP train) to a larger extent (***D***; baseline; $n = 5$). *$p < 0.05$; **$p < 0.01$ (two-way ANOVA with Bonferroni's test). This larger temporal summation and depolarization of AOB inputs was substantially reduced after application of D-APV (***C***, ***D***). All graph bars are mean ± SEM.

Pathway-specific spatial segregation of excitatory synapses on dendrites has been described previously in cortical and hippocampal pyramidal neurons (Amaral, 1993; Haberly, 2001; Spruston, 2008), but not in the amygdala, which, with the exception of the CoA, lacks a clear laminar organization. Thus far, the only evidence for afferent-specific segregation of excitatory synapses in the amygdala has been at the level of neighboring, but distinct, dendritic spines on projection neurons of the lateral amygdala (Humeau et al., 2005). Interestingly, our data suggest that the organization of olfactory input to MeA principal cells is similar to that for layer II/III principal neurons in the piriform cortex. Thus, afferents from the main olfactory bulb carried in the lateral olfactory tract (LOT) synapse onto the distal apical dendrites in layer Ia of the piriform cortex (Haberly, 2001), resembling AOB synapses on distal dendrites of MePV principal cells in the molecular layer. Associational synapses, on the other hand, are formed closer to the soma in deeper layers of the piriform cortex (Johnson et al., 2000), comparable to CoA synapses on proximal dendritic domains of MePV neurons. Consistent with our findings in the MePV, in layer II/III pyramidal neurons, somatic recordings of LOT and associational inputs have different kinetics, with slower rise and decay times for the distal LOT input, due to greater electrotonic filtering (Franks and Isaacson, 2005). Moreover, differences in short-term plasticity between LOT and associational inputs to the semipyramidal cells of the piriform cortex (Bower and Haberly, 1986; Franks and Isaacson, 2005; Suzuki and Bekkers, 2006) were also found between AOB and CoA inputs, with paired-pulse facilitation at AOB but not CoA synapses. Together, these findings indicate that the olfactory processing circuitry in the MeA is homologous to that in the piriform cortex.

Considering that AOB synapses provide the major flow of sensory information to the MeA, their electrotonically disadvantaged location on distal dendrites raises the question of whether any compensatory mechanism is used to amplify their output gain. A number of passive and active dendritic properties have been suggested to enhance the efficacy of distal synapses (Schiller et al., 1997; Magee and Cook, 2000; Williams and Stuart, 2002; Larkum et al., 2009), and even to confer on them a larger impact on the soma than proximal synapses (Branco and Häusser, 2011). Excitatory inputs to distal cortical dendrites, for instance, were shown to integrate over a wider temporal window and be amplified with a higher gain than proximal inputs, largely due to the recruitment of distal NMDARs (Branco and Häusser, 2011). Our results demonstrating NMDAR-dependent broad temporal summation and a higher output gain of distal AOB inputs are in line with these findings. Moreover, consistent with larger NMDAR activation by unsynchronized AOB inputs, Ca^{2+} transients were more readily evoked by AOB than CoA EPSPs. Interestingly, our finding that successive AOB inputs are more effective than CoA inputs in discharging MeA neurons also corresponds to the previous *in vivo* data showing that these neurons can be driven by stimulation of the vomeronasal organ, but not the main olfactory epithelium (Bergan et al., 2014).

The NMDAR dependence of AOB input summation may be explained by the high input impedance at distal synapses, which would cause a relatively larger local dendritic depolarization at these sites and release the magnesium block of NMDARs (Nowak et al., 1984; Schiller et al., 1997; Larkum et al., 2009; Branco and

Häusser, 2011). Moreover, other contributing mechanisms may include differences in the number, density, or subunit composition of NMDARs at these two synapses (Otmakhova et al., 2002; Nicholson et al., 2006). Previous data suggest that, in contrast to synapses in the MOB, a large number of AOB synapses are rich in the GluN2B subunit of NMDARs (Dani et al., 2010). Whether similar rules apply to AOB and CoA synapses on MeA neurons awaits future studies using dendritic recording (Andrasfalvy and Magee, 2001) or nanoscale imaging of labeled glutamate receptors at these synapses (Nicholson et al., 2006; Dani et al., 2010). Moreover, potential spillover of glutamate to neighboring extrasynaptic NMDARs, which is thought to promote the generation of dendritic NMDA spikes (Chalifoux and Carter, 2011), may also play a part. Finally as shown in Figure 1, both inputs evoke clear inhibitory responses, mediated by local feedforward inhibition (Keshavarzi et al., 2014). Although not tested in the current study, differential recruitment of these inhibitory inputs will also likely play a role in processing these inputs *in vivo*.

What is the functional outcome of this wiring for olfactory processing in the MeA? Previous studies in pyramidal neurons have shown that distal synapses can impact the gain and plasticity of proximal inputs (Remondes and Schuman, 2002; Dudman et al., 2007; Han and Heinemann, 2013). In CA1 pyramidal neurons, for instance, closely timed activation of the distal perforant path and the proximal Schaffer-collateral synapses induces potentiation of the latter (Dudman et al., 2007). Thus, it is likely that, through a similar mechanism, an association between main and accessory olfactory inputs will be formed in MeA principal neurons, leading to odor-evoked responses driven by pheromonal cues. In line with this hypothesis, intact accessory olfactory signaling was found to be necessary for normal mating behavior in sexually inexperienced male hamsters, whereas once mated or preexposed to female chemosignals, the main olfactory system alone was sufficient (Meredith, 1986; Westberry and Meredith, 2003), indicating that odors can be learnt in association with pheromones through experience. We thus propose that future studies address this hypothesis by investigating the interaction between main and accessory olfactory inputs at the level of individual MeA neurons and in behavior.

References

Amaral DG (1993) Emerging principles of intrinsic hippocampal organization. Curr Opin Neurobiol 3:225–229. Medline

Andrasfalvy BK, Magee JC (2001) Distance-dependent increase in AMPA receptor number in the dendrites of adult hippocampal CA1 pyramidal neurons. J Neurosci 21:9151–9159. Medline

Bathellier B, Margrie TW, Larkum ME (2009) Properties of piriform cortex pyramidal cell dendrites: implications for olfactory circuit design. J Neurosci 29:12641–12652. CrossRef Medline

Ben-Shaul Y, Katz LC, Mooney R, Dulac C (2010) *In vivo* vomeronasal stimulation reveals sensory encoding of conspecific and allospecific cues by the mouse accessory olfactory bulb. Proc Natl Acad Sci U S A 107:5172–5177. CrossRef Medline

Bergan JF, Ben-Shaul Y, Dulac C (2014) Sex-specific processing of social cues in the medial amygdala. Elife 3:e02743. Medline

Bian X, Yanagawa Y, Chen WR, Luo M (2008) Cortical-like functional organization of the pheromone-processing circuits in the medial amygdala. J Neurophysiol 99:77–86. Medline

Binns KE, Brennan PA (2005) Changes in electrophysiological activity in the accessory olfactory bulb and medial amygdala associated with mate recognition in mice. Eur J Neurosci 21:2529–2537. Medline

Bower JM, Haberly LB (1986) Facilitating and nonfacilitating synapses on pyramidal cells: a correlation between physiology and morphology. Proc Natl Acad Sci U S A 83:1115–1119. CrossRef Medline

Branco T, Häusser M (2011) Synaptic integration gradients in single cortical pyramidal cell dendrites. Neuron 69:885–892. CrossRef Medline

Brennan PA, Zufall F (2006) Pheromonal communication in vertebrates. Nature 444:308–315. CrossRef Medline

Cádiz-Moretti B, Otero-García M, Martínez-García F, Lanuza E (2014) Afferent projections to the different medial amygdala subdivisions: a retrograde tracing study in the mouse. Brain Struct Funct. Advance online publication. CrossRef Medline

Canteras NS, Simerly RB, Swanson LW (1995) Organization of projections from the medial nucleus of the amygdala: a PHAL study in the rat. J Comp Neurol 360:213–245. Medline

Chalifoux JR, Carter AG (2011) Glutamate spillover promotes the generation of NMDA spikes. J Neurosci 31:16435–16446. CrossRef Medline

Choi GB, Dong HW, Murphy AJ, Valenzuela DM, Yancopoulos GD, Swanson LW, Anderson DJ (2005) Lhx6 delineates a pathway mediating innate reproductive behaviors from the amygdala to the hypothalamus. Neuron 46:647–660. CrossRef Medline

Colbert CM, Levy WB (1992) Electrophysiological and pharmacological characterization of perforant path synapses in CA1: mediation by glutamate receptors. J Neurophysiol 68:1–8. Medline

Cooke BM, Woolley CS (2005) Sexually dimorphic synaptic organization of the medial amygdala. J Neurosci 25:10759–10767. CrossRef Medline

Cooke BM, Stokas MR, Woolley CS (2007) Morphological sex differences and laterality in the prepubertal medial amygdala. J Comp Neurol 501:904–915. Medline

Dani A, Huang B, Bergan J, Dulac C, Zhuang X (2010) Superresolution imaging of chemical synapses in the brain. Neuron 68:843–856. CrossRef Medline

Dudman JT, Tsay D, Siegelbaum SA (2007) A role for synaptic inputs at distal dendrites: instructive signals for hippocampal long-term plasticity. Neuron 56:866–879. CrossRef Medline

Fernandez-Fewell GD, Meredith M (1994) c-fos expression in vomeronasal pathways of mated or pheromone-stimulated male golden hamsters: contributions from vomeronasal sensory input and expression related to mating performance. J Neurosci 14:3643–3654. Medline

Franks KM, Isaacson JS (2005) Synapse-specific downregulation of NMDA receptors by early experience: a critical period for plasticity of sensory input to olfactory cortex. Neuron 47:101–114. CrossRef Medline

Golding NL, Spruston N (1998) Dendritic sodium spikes are variable triggers of axonal action potentials in hippocampal CA1 pyramidal neurons. Neuron 21:1189–1200. CrossRef Medline

Govic A, Paolini AG (2015) *In vivo* electrophysiological recordings in amygdala subnuclei reveal selective and distinct responses to a behaviorally identified predator odor. J Neurophysiol 113:1423–1436. CrossRef Medline

Haberly LB (2001) Parallel-distributed processing in olfactory cortex: new insights from morphological and physiological analysis of neuronal circuitry. Chem Senses 26:551–576. CrossRef Medline

Han EB, Heinemann SF (2013) Distal dendritic inputs control neuronal activity by heterosynaptic potentiation of proximal inputs. J Neurosci 33:1314–1325. CrossRef Medline

Helmchen F, Svoboda K, Denk W, Tank DW (1999) *In vivo* dendritic calcium dynamics in deep-layer cortical pyramidal neurons. Nat Neurosci 2:989–996. Medline

Humeau Y, Herry C, Kemp N, Shaban H, Fourcaudot E, Bissière S, Lüthi A (2005) Dendritic spine heterogeneity determines afferent-specific Hebbian plasticity in the amygdala. Neuron 45:119–131. CrossRef Medline

Johnson DM, Illig KR, Behan M, Haberly LB (2000) New features of connectivity in piriform cortex visualized by intracellular injection of pyramidal cells suggest that "primary" olfactory cortex functions like "association" cortex in other sensory systems. J Neurosci 20:6974–6982. Medline

Kampa BM, Letzkus JJ, Stuart GJ (2007) Dendritic mechanisms controlling spike-timing-dependent synaptic plasticity. Trends Neurosci 30:456–463. Medline

Kang N, Baum MJ, Cherry JA (2009) A direct main olfactory bulb projection to the 'vomeronasal' amygdala in female mice selectively responds to volatile pheromones from males. Eur J Neurosci 29:624–634. Medline

Keshavarzi S, Sullivan RKP, Ianno DJ, Sah P (2014) Functional properties and projections of neurons in the medial amygdala. J Neurosci 34:8699–8715. CrossRef Medline

Kevetter GA, Winans SS (1981) Connections of the corticomedial amygdala in the golden hamster. II. Efferents of the "olfactory amygdala." J Comp Neurol 197:99–111. Medline

Larkum ME, Nevian T, Sandler M, Polsky A, Schiller J (2009) Synaptic integration in tuft dendrites of layer 5 pyramidal neurons: a new unifying principle. Science 325:756–760. CrossRef Medline

Lau CG, Murthy VN (2012) Activity-dependent regulation of inhibition via GAD67. J Neurosci 32:8521–8531. CrossRef Medline

Lehman MN, Winans SS, Powers JB (1980) Medial nucleus of the amygdala mediates chemosensory control of male hamster sexual behavior. Science 210:557–560. CrossRef Medline

Li CI, Maglinao TL, Takahashi LK (2004) Medial amygdala modulation of predator odor-induced unconditioned fear in the rat. Behav Neurosci 118:324–332. Medline

Licht G, Meredith M (1987) Convergence of main and accessory olfactory pathways onto single neurons in the hamster amygdala. Exp Brain Res 69:7–18. Medline

London M, Häusser M (2005) Dendritic computation. Annu Rev Neurosci 28:503–532. Medline

Magee JC (2000) Dendritic integration of excitatory synaptic input. Nat Rev Neurosci 1:181–190. Medline

Magee JC, Cook EP (2000) Somatic EPSP amplitude is independent of synapse location in hippocampal pyramidal neurons. Nat Neurosci 3:895–903. Medline

Martinez-Marcos A (2009) On the organization of olfactory and vomeronasal cortices. Prog Neurobiol 87:21–30. Medline

McDonald AJ (1998) Cortical pathways to the mammalian amygdala. Prog Neurobiol 55:257–332. Medline

McGregor IS, Hargreaves GA, Apfelbach R, Hunt GE (2004) Neural correlates of cat odor-induced anxiety in rats: region-specific effects of the benzodiazepine midazolam. J Neurosci 24:4134–4144. CrossRef Medline

Meredith M (1986) Vomeronasal organ removal before sexual experience impairs male hamster mating behavior. Physiol Behav 36:737–743. Medline

Miyamichi K, Amat F, Moussavi F, Wang C, Wickersham I, Wall NR, Taniguchi H, Tasic B, Huang ZJ, He Z, Callaway EM, Horowitz MA, Luo L (2011) Cortical representations of olfactory input by trans-synaptic tracing. Nature 472:191–196. CrossRef Medline

Mohedano-Moriano A, Pro-Sistiaga P, Ubeda-BañónI, Crespo C, Insausti R, Martinez-Marcos A (2007) Segregated pathways to the vomeronasal amygdala: differential projections from the anterior and posterior divisions of the accessory olfactory bulb. Eur J Neurosci 25:2065–2080. Medline

Nicholson DA, Trana R, Katz Y, Kath WL, Spruston N, Geinisman Y (2006) Distance-dependent differences in synapse number and AMPA receptor expression in hippocampal CA1 pyramidal neurons. Neuron 50:431–442. CrossRef Medline

Nowak L, Bregestovski P, Ascher P, Herbet A, Prochiantz A (1984) Magnesium gates glutamate-activated channels in mouse central neurones. Nature 307:462–465. CrossRef Medline

Oh SW, Harris JA, Ng L, Winslow B, Cain N, Mihalas S, Wang Q, Lau C, Kuan L, Henry AM, Mortrud MT, Ouellette B, Nguyen TN, Sorensen SA, Slaughterbeck CR, Wakeman W, Li Y, Feng D, Ho A, Nicholas E, et al. (2014) A mesoscale connectome of the mouse brain. Nature 508:207–214. CrossRef Medline

Otmakhova NA, Otmakhov N, Lisman JE (2002) Pathway-specific properties of AMPA and NMDA-mediated transmission in CA1 hippocampal pyramidal cells. J Neurosci 22:1199–1207. Medline

Papes F, Logan DW, Stowers L (2010) The vomeronasal organ mediates interspecies defensive behaviors through detection of protein pheromone homologs. Cell 141:692–703. CrossRef Medline

Pare D, Duvarci S (2012) Amygdala microcircuits mediating fear expression and extinction. Curr Opin Neurobiol 22:717–723. Medline

Paxinos G, Franklin BJ (2001) The mouse brain in stereotaxic coordinates, Ed 2. San Diego: Academic.

Phelps EA, LeDoux JE (2005) Contributions of the amygdala to emotion processing: from animal models to human behavior. Neuron 48:175–187. CrossRef Medline

Pro-Sistiaga P, Mohedano-Moriano A, Ubeda-Bañon I, Del Mar Arroyo-Jimenez M, Marcos P, Artacho-Pérula E, Crespo C, Insausti R, Martinez-Marcos A (2007) Convergence of olfactory and vomeronasal projections in the rat basal telencephalon. J Comp Neurol 504:346–362. Medline

Rall W (1964) Theoretical significance of dendritic trees for neuronal input-output relations. In: Neural theory and modeling (Reiss RF, ed), pp 73–97. Stanford, CA: Stanford UP.

Rall W (1967) Distinguishing theoretical synaptic potentials computed for different soma-dendritic distributions of synaptic input. J Neurophysiol 30:1138–1168. Medline

Rasia-Filho AA, Fabian C, Rigoti KM, Achaval M (2004) Influence of sex, estrous cycle and motherhood on dendritic spine density in the rat medial amygdala revealed by the Golgi method. Neuroscience 126:839–847. CrossRef Medline

Remondes M, Schuman EM (2002) Direct cortical input modulates plasticity and spiking in CA1 pyramidal neurons. Nature 416:736–740. CrossRef Medline

Samuelsen CL, Meredith M (2009) The vomeronasal organ is required for the male mouse medial amygdala response to chemical-communication signals, as assessed by immediate early gene expression. Neuroscience 164:1468–1476. CrossRef Medline

Samuelsen CL, Meredith M (2011) Oxytocin antagonist disrupts male mouse medial amygdala response to chemical-communication signals. Neuroscience 180:96–104. CrossRef Medline

Scalia F, Winans SS (1975) The differential projections of the olfactory bulb and accessory olfactory bulb in mammals. J Comp Neurol 161:31–55. Medline

Schiller J, Schiller Y, Stuart G, Sakmann B (1997) Calcium action potentials restricted to distal apical dendrites of rat neocortical pyramidal neurons. J Physiol 505:605–616. Medline

Schindelin J, Arganda-Carreras I, Frise E, Kaynig V, Longair M, Pietzsch T, Preibisch S, Rueden C, Saalfeld S, Schmid B, Tinevez JY, White DJ, Hartenstein V, Eliceiri K, Tomancak P, Cardona A (2012) Fiji: an open-source platform for biological-image analysis. Nat Methods 9:676–682. Medline

Sosulski DL, Bloom ML, Cutforth T, Axel R, Datta SR (2011) Distinct representations of olfactory information in different cortical centres. Nature 472:213–216. CrossRef Medline

Spruston N (2008) Pyramidal neurons: dendritic structure and synaptic integration. Nat Rev Neurosci 9:206–221. Medline

Spruston N, Schiller Y, Stuart G, Sakmann B (1995) Activity-dependent action potential invasion and calcium influx into hippocampal CA1 dendrites. Science 268:297–300. CrossRef Medline

Stowers L, Cameron P, Keller JA (2013) Ominous odors: olfactory control of instinctive fear and aggression in mice. Curr Opin Neurobiol 23:339–345. Medline

Stuart GJ, Dodt HU, Sakmann B (1993) Patch-clamp recordings from the soma and dendrites of neurons in brain slices using infrared video microscopy. Pflugers Arch 423:511–518. Medline

Suzuki N, Bekkers JM (2006) Neural coding by two classes of principal cells in the mouse piriform cortex. J Neurosci 26:11938–11947. CrossRef Medline

Swanson LW (2000) Cerebral hemisphere regulation of motivated behavior. Brain Res 886:113–164. Medline

Tamamaki N, Yanagawa Y, Tomioka R, Miyazaki J, Obata K, Kaneko T (2003) Green fluorescent protein expression and colocalization with calretinin, parvalbumin, and somatostatin in the GAD67-GFP knock-in mouse. J Comp Neurol 467:60–79. Medline

von Campenhausen H, Mori K (2000) Convergence of segregated pheromonal pathways from the accessory olfactory bulb to the cortex in the mouse. Eur J Neurosci 12:33–46. Medline

Westberry JM, Meredith M (2003) Pre-exposure to female chemosignals or intracerebral GnRH restores mating behavior in naive male hamsters with vomeronasal organ lesions. Chem Senses 28:191–196. CrossRef Medline

Williams SR, Stuart GJ (2002) Dependence of EPSP efficacy on synapse location in neocortical pyramidal neurons. Science 295:1907–1910. CrossRef Medline

Williams SR, Stuart GJ (2003) Role of dendritic synapse location in the control of action potential output. Trends Neurosci 26:147–154. Medline